Structural disorder-induced topological phase transitions in quasicrystals

Tan Peng [1,2,*] Yong-Chen Xiong,[2,*] Chun-Bo Hua [3] Zheng-Rong Liu [4] Xiaolu Zhu [1] Wei Cao,[1,5] Fang Lv,[1] Yue Hou,[5] Bin Zhou [4,6,†] Ziyu Wang [1,5,‡] and Rui Xiong[1,§]

[1]*Key Laboratory of Artificial Micro- and Nano-Structures of Ministry of Education, School of Physics and Technology, Wuhan University, Wuhan 430072, China*

[2]*Hubei Key Laboratory of Energy Storage and Power Battery and School of Mathematics, Physics and Optoelectronic Engineering, Hubei University of Automotive Technology, Shiyan 442002, China*

[3]*School of Electronic and Information Engineering, Hubei University of Science and Technology, Xianning 437100, China*

[4]*Department of Physics, Hubei University, Wuhan 430062, China*

[5]*The Institute of Technological Science, Wuhan University, Wuhan 430072, China*

[6]*Key Laboratory of Intelligent Sensing System and Security of Ministry of Education, Hubei University, Wuhan 430062, China*

(Received 31 December 2023; revised 28 April 2024; accepted 2 May 2024; published 14 May 2024)

Recently, structural disorder-induced topological phase transitions in periodic systems have attracted much attention. However, in aperiodic systems such as quasicrystalline systems, the interplay between structural disorder and band topology is still unclear. In this work, we investigate the effects of structural disorder on a quantum spin Hall insulator phase and a higher-order topological phase in a two-dimensional Amman-Beenker tiling quasicrystalline lattice. We demonstrate that the structural disorder can induce a topological phase transition from a quasicrystalline normal insulator phase to an amorphous quantum spin Hall insulator phase, which is confirmed by bulk gap closing and reopening, robust edge states, a quantized spin Bott index, and conductance. Furthermore, the structural disorder-induced higher-order topological phase transition from a quasicrystalline normal insulator phase to an amorphous higher-order topological phase characterized by a quantized quadrupole moment and topological corner states is also found. More strikingly, the disorder-induced higher-order topological insulator with eight corner states represents a distinctive topological state that eludes realization in conventional crystalline systems. Our work extends the study of the interplay between disorder effects and topologies to quasicrystalline and amorphous systems.

DOI: 10.1103/PhysRevB.109.195301

I. INTRODUCTION

Numerous factors can instigate topological phase transitions (TPTs) [1–6], and notably, disorder-induced TPTs have attracted significant attention. This stems from the inherent presence of disorder to varying degrees in real materials. Anderson-type on-site disorder, which is typically utilized to modulate the topological properties of electronic wave functions by altering the electronic chemical potential, leading to the theoretical prediction of the topological Anderson insulator as well as higher-order topological Anderson insulators in various condensed matter systems [7–30], is widely employed to induce TPTs. However, due to the stringent requirements of experimental conditions, the topological Anderson insulator and higher-order topological Anderson insulators have been achieved in only one-dimensional ultracold atomic wires [31] and simulated experiments based on photonic crystals [32–34], phononic crystals [35], and the electric circuit setup [36].

Recently, the TPT induced by structural disorder has attracted widespread attention. For instance, Li *et al.* proposed a TPT induced by the structural disorder in a one-dimensional amorphous Rydberg atom chain [37]. Later, the structural disorder was used to induced a second-order topological insulator phase with topological hinge states in a three-dimensional cubical lattice [38], and a quantum spin Hall insulator phase with topological edge states in a two-dimensional trigonal lattice [39] was proposed. The origin of structural disorder-induced TPTs is the renormalization of spectral gaps associated with single-particle energy levels, resulting in potential changes in the energy levels and spectral gaps of electrons [39]. Therefore, the physical mechanisms of TPTs induced by structural disorder and Anderson-type on-site disorder are fundamentally different, with the latter arising from many-body effects, as the fluctuation of on-site energies is intricately linked to electron-electron interactions [39]. From a theoretical perspective, one direct approach to introducing structural disorder is to add a random displacement of varying magnitudes to each lattice point, causing the original lattice points to deviate from their initial positions, and is accompanied by the amorphization of the material [38,39]. The attractiveness of TPTs induced by structural disorder can be ascribed to two main reasons. First, amorphous structures are ubiquitous in the natural world [40].

*These authors contributed equally to this work.
†binzhou@hubu.edu.cn
‡zywang@whu.edu.cn
§xiongrui@whu.edu.cn

Second, nearly all materials can be prepared in amorphous phases through various amorphization techniques [41–48]. Therefore, combining TPTs with structural disorder allows for observation in experiments using a wide range of selectable materials.

Quasicrystalline systems present new opportunities for exploring novel topological states associated with high rotational symmetry, which is forbidden in crystals, such as the fivefold [49], eightfold [50], and 12-fold [51] rotational symmetries. So far, the TPTs induced by Anderson-type onsite disorder in quasicrystalline systems have been extensively studied [29,52–56]. Furthermore, several researches have investigated TPTs induced by structural disorder in the context of a periodic lattice framework [38,39,57]. However, it is not yet clear whether structural disorder can induce TPTs in quasiperiodic lattice systems.

In this paper, we investigate the structural disorder-induced TPTs in an Ammann-Beenker tiling octagonal quasicrystal. In the case of the TPT from a quasicrystalline normal insulator phase to an amorphous quantum spin Hall insulator phase, by calculating the real-space spin Bott index [58,59], two-terminal conductance [60–62], and the probability density of the in-gap eigenstates, we find that the topologically trivial phase changes to a topologically nontrivial phase characterized by a nonzero spin Bott index ($B_s = 1$) with a quantized conductance plateau ($G = 2e^2/h$) in a certain range of disorder strength. Furthermore, by calculating the real-space quadrupole moment [27,28,63–66] and the probability distribution of in-gap states, we also identify a structural disorder-induced TPT from an initial quasicrystalline topologically trivial phase to an amorphous higher-order topological phase occurring in a certain range of disorder strength with four localized gapless corner states characterized by a quantized quadrupole moment ($q_{xy} = 0.5$). Even more remarkable is the discovery of a structural disorder-induced higher-order topological insulator phase, characterized by eight localized gapless corner states confined within an octagonal boundary, representing a distinctive topological state that eludes realization in conventional crystalline systems.

The rest of this paper is organized as follows. We introduce a quantum spin Hall insulator model and a higher-order insulator model with structural disorder in a two-dimensional quasicrystalline lattice and give the details of the numerical methods in Sec. II. Then, we provide the numerical results of studying the TPTs of the two models in Secs. III and IV. Finally, we summarize our conclusions in Sec. V.

II. MODELS AND METHOD

We start with a tight-binding model of a quantum spin Hall insulator in an Ammann-Beenker tiling quasicrystalline lattice [67–70] with square boundary conditions, as shown in Fig. 1(a). The quasicrystal structure is formed by the aperiodic arrangement of squares and rhombi with equal side lengths in a two-dimensional plane. We consider the first three nearest-neighbor hoppings, i.e., the short diagonal of the rhombus, the edge of the rhombus and square, and the diagonal of the square. The model Hamiltonian is

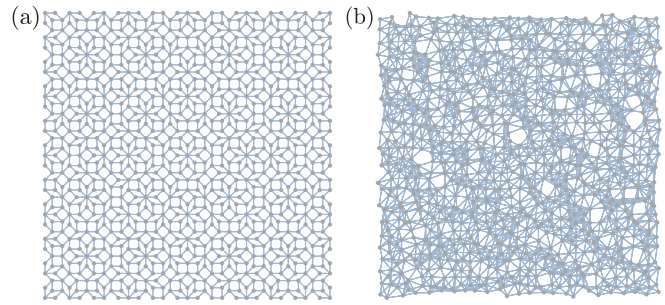

FIG. 1. (a) Schematic diagram of the Ammann-Beenker tiling quasicrystal containing 1005 sites. The first three nearest-neighbor intercell bonds correspond to the short diagonal of the rhombus tile, the edge of the square and rhombus tile, and the diagonal of the square tile, respectively. The distance ratio of the three bonds is $r_0 : r_1 : r_2 = 2\sin\frac{\pi}{8} : 1 : 2\sin\frac{\pi}{4}$. (b) The Ammann-Beenker tiling quasicrystal transforms into an amorphous structure in the presence of structural disorder, where the strength of disorder is $\sigma = 0.2$. We set the hopping radius as $R = 1.7$, ensuring the first three nearest-neighbor hoppings in the quasicrystalline structure. To clearly depict the quasicrystalline structure, only the second-order nearest-neighbor bonds are illustrated in (a).

given by

$$H = -\sum_{m\neq n}\frac{l(r_{mn})}{2}c_m^\dagger[it_1(s_3\tau_1\cos\psi_{mn} + s_0\tau_2\sin\psi_{mn}) + t_2 s_0\tau_3]c_n + \sum_m (M + 2t_2)c_m^\dagger s_0\tau_3 c_m, \quad (1)$$

where $c_m^\dagger = (c_{m\alpha\uparrow}^\dagger, c_{m\alpha\downarrow}^\dagger, c_{m\beta\uparrow}^\dagger, c_{m\beta\downarrow}^\dagger)$ represents the creation operator of an electron on a site m. m and n denote lattice sites running from 1 to N, and N is the total number of lattice sites. In each site, α and β are the indices of the orbitals, and $\uparrow$ and $\downarrow$ represent the spin direction. $s_{1,2,3}$ and $\tau_{1,2,3}$ are the Pauli matrices acting on the spin and orbital degrees of freedom, respectively. s_0 and τ_0 are the 2×2 identity matrices. $t_{1,2}$ are the hopping strengths, and M is the Dirac mass. ψ_{mn} is the polar angle of the bond between sites m and n with respect to the horizontal direction. $l(r_{mn}) = e^{1-r_{mn}/\lambda}$ is the spatial decay factor of the hopping amplitudes, with λ being the decay length, where $r_{mn} = |\mathbf{r}_m - \mathbf{r}_n|$ is the distance from site m to site n. The model Hamiltonian preserves time-reversal symmetry T, particle-hole symmetry P, and chiral symmetry S; therefore, it belongs to class DIII [71,72]. Here, the symmetry operators are $T = is_2\tau_0 K$, $P = s_3\tau_1 K$, and $S = TP$, respectively, where K is the complex conjugate operator. Furthermore, when the Hamiltonian (1) is projected onto a square lattice with exclusive consideration of nearest-neighbor hopping, the model will evolve into a quantum spin Hall insulator based on HgTe quantum wells [73]. Without loss of generality, the spatial decay length λ and the side length of the rhombus and square r_1 are fixed to 1, and the energy unit is set as $t_1 = t_2 = 1$.

In order to investigate TPTs in a quasicrystalline lattice with varying degrees of structural disorder, we considered the atomic thermal fluctuations corresponding to the typical quenching process of a molten state. The specific approach involves adding a displacement $\mathbf{r}$ at each lattice point in the quasicrystal structure with a randomly determined magnitude

and direction, where the magnitude follows a Gaussian distribution [39,74]. The random displacement can be written as

$$D(\mathbf{r}) = \frac{1}{2\pi\sigma^2}\exp\left(-\frac{r^2}{2\sigma^2}\right), \tag{2}$$

where the distance standard deviation σ is the intensity of structural disorder, which is scaled in units of the edge of the rhombus and square. In Fig. 1(b), we plot the Ammann-Beenker tiling quasicrystal in the presence of structural disorder with the strength of the disorder being $\sigma = 0.2$, where the quasicrystalline structure has been converted to an amorphous structure.

To characterize the structural disorder-induced amorphous quantum spin Hall insulator phase, we adopt the spin Bott index [58,59] as well as the two-terminal conductance based on the recursive Green's function method [75,76]. The detailed steps of the numerical calculation of the spin Bott index can be summed up as follows. First, one constructs the projector operator of the occupied states as $P = \sum_i^{N_{\rm occ}} |\psi_i\rangle\langle\psi_i|$, where ψ_i is the ith wave function of the Hamiltonian (1) and $N_{\rm occ}$ is the total number of occupied states. Second, one introduces another projector operator as $P_z = P\hat{\eta}_z P$, where $\hat{\eta}_z = \frac{\hbar}{2}s_3$ is the spin operator with the Pauli matrix s_3. The eigenvalues of P_z are divided into two parts by zero energy, in which the number of positive and negative eigenvalues are both equal to $N_{\rm occ}/2$. Then, a new projector operator can be constructed as $P_\pm = \sum_i^{N/2} |\phi_i^\pm\rangle\langle\phi_i^\pm|$. The projected position operators of the two spin sectors can be defined as

$$U_\pm = P_\pm e^{i2\pi X} P_\pm + (I - P_\pm), \tag{3}$$

$$V_\pm = P_\pm e^{i2\pi Y} P_\pm + (I - P_\pm), \tag{4}$$

where X and Y are two diagonal matrices, $X_{ii} = x_i/L_x$ and $Y_{ii} = y_i/L_y$, with (x_i, y_i) being the coordinate of the ith lattice site and $L_{x(y)}$ being the size of the sample along the x (y) direction. Finally, one can obtain the spin Bott index as

$$B_s = \tfrac{1}{2}(B_+ - B_-), \tag{5}$$

where $B_\pm = \frac{1}{2\pi}\mathrm{Im}\{\mathrm{Tr}[\ln(\tilde{V}_\pm\tilde{U}_\pm\tilde{V}_\pm^\dagger\tilde{U}_\pm^\dagger)]\}$ are the Bott indexes of up and down spins, respectively. The case with $B_s = 0$ corresponds to the normal insulator phase, and $B_s = 1$ corresponds to the quantum spin Hall insulator phase. We note that the calculation of B_s is performed in the framework of periodic boundary conditions constructed using quasiperiodic approximation theory [77–79].

Moreover, according to the Landauer-Büttiker-Fisher-Lee formula [60–62], the conductance can be written as

$$G = \frac{e^2}{h}T(\mu), \tag{6}$$

where $T(\mu) = \mathrm{Tr}[\Gamma_L(\mu)G^r(\mu)\Gamma_R(\mu)G^a(\mu)]$ is the transmission coefficient at energy μ. $\Gamma_{L(R)}(\mu) = i(\Sigma^r_{L(R)} - \Sigma^a_{L(R)})$ is the left (right) linewidth with the left (right) lead retarded self-energy $\Sigma^r_{L(R)}$ and the left (right) lead advanced self-energy $\Sigma^a_{L(R)}$. $G^{r(a)}(\mu)$ is the retarded (advanced) Green's function of the device and can be expressed as

$$G^r(\mu) = [G^a(\mu)]^\dagger = \left[\mu - H_d - \Sigma_L^r - \Sigma_R^r\right]^{-1}, \tag{7}$$

where H_d is the device Hamiltonian. For a quantum spin Hall insulator phase, the two-terminal conductance is a quantized number $G = 2e^2/h$, and $G = 0$ corresponds to a normal insulator phase.

It has been proposed that the Wilson mass term can destroy the time-reversal symmetry of the quantum spin Hall insulator which is described by Hamiltonian (1), so that the original helical boundary state of the system opens the energy gap and evolves into a higher-order corner state [50]. The mass term can be written as

$$H_g = -g\sum_{m\neq n}\frac{l(r_{mn})}{2}c_m^\dagger s_1\tau_1\cos(\xi\psi_{mn})c_n, \tag{8}$$

where g is the magnitude of the mass term, ξ is the varying period of the mass term, and $\xi = 2$ (4) for square (octagonal) samples.

To describe higher-order topological phases in an aperiodic lattice, we will employ a topologically invariant real-space quadrupole moment [27,28,63–66]. The form of the real-space quadrupole moment is

$$q_{xy} = \frac{1}{2\pi}\mathrm{Im}\ln[\det(\Psi_{\rm occ}^\dagger\hat{U}\Psi_{\rm occ})\sqrt{\det(\hat{U}^\dagger)}], \tag{9}$$

where $\Psi_{\rm occ}$ is the eigenvectors of occupied states. $\hat{U} \equiv \exp[i2\pi\hat{X}\hat{Y}/L^2]$, where $\hat{X}$ and $\hat{Y}$ are the position operators and L represents the side length of the sample. In the case of $q_{xy} = 0.5$, the system is a second-order topological phase with topological corner states. IN addition, $q_{xy} = 0$ indicates a trivial phase. Note that the subsequent calculations of q_{xy} in this paper are based on periodic boundary conditions.

In addition, another suitable method for characterizing higher-order topological phases is to use the existence of corner states as a criterion for determination [29,36,80–82]. In the subsequent computations related to disorder-induced higher-order topological phases, we determine the topology of the system by computing the real-space topological invariant q_{xy} and determining the presence of corner states.

III. STRUCTURAL DISORDER-INDUCED FIRST-ORDER TOPOLOGICAL PHASE

In this section, we focus on the structural disorder-induced first-order topological insulator phase in an Ammann-Beenker tiling quasicrystal with square boundary conditions. We have confirmed that even in the presence of structural disorder, symmetries such as time-reversal symmetry, particle-hole symmetry, and chiral symmetry remain preserved.

Figure 2(a) shows the spin Bott index B_s as a function of disorder strength σ and Dirac mass M. The color map shows the magnitude of the spin Bott index. In the clean limit, i.e., $\sigma = 0$, the quasicrystalline lattice hosts a normal insulator phase characterized by $B_s = 0$ with the parameter $1.55 < M < 2$. However, as the strength of structural disorder increases from zero, the normal insulator phase converts to a topological insulator phase characterized by $B_s = 1$. It is noted that the TPTs are limited to the region $1.55 < M < 2$. Additionally, we observe that the critical disorder strength σ_c of the TPTs increases with the growth of M.

It is well known that the process of TPT is inevitably accompanied by the closing and reopening of the bulk energy

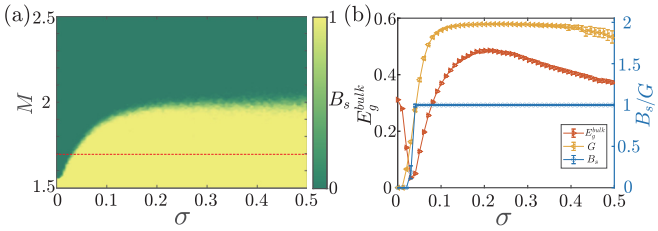

FIG. 2. (a) Topological phase diagram of the Ammann-Beenker tiling quasicrystal in (M, σ) space obtained by calculating the real-space topologically invariant spin Bott index B_s. The yellow color represents the topological insulator phase corresponding to $B_s = 1$, and the green color represents the normal insulator phase corresponding to $B_s = 0$. The red dashed line represents $M = 1.7$. (b) Bulk energy gap E_g^{bulk}, spin Bott index B_s, and two-terminal conductance G versus disorder strength σ with $M = 1.7$. The system with PBCs marked by the orange line shows that the bulk energy gap has undergone the process of closing and reopening. The system contains 1005 sites, and 500 disorder configurations are made.

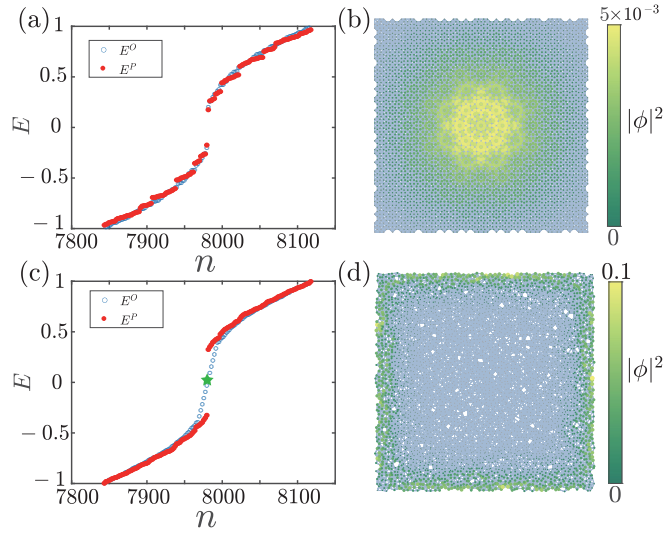

FIG. 3. (a) Energy spectrum of the normal insulator with open boundary conditions (marked by blue circles) and periodic boundary conditions (marked by red circles), corresponding to the situation with $\sigma = 0$ in Fig. 2(b). (b) The probability density of the four eigenstates which are the nearest to zero energy in (a). (c) Energy spectrum of the topological insulator corresponding to the situation with $\sigma = 0.18$ in Fig. 2(b). (d) The probability density of the edge states marked by green star. To mitigate the finite-size effect, the system size is set to contain 4061 sites, and $M = 1.7$. The color bar represents the magnitude of the probability of the wave function $|\phi|^2$.

gap, and the point where the gap closes represents the critical point of the phase transition. In general, the energy gap of a system with periodic boundary conditions is equal to the bulk energy gap. However, for aperiodic systems, it is necessary to employ quasiperiodic approximation theory to construct periodic boundary conditions. In Fig. 2(b), we plot the bulk energy gap versus disorder strength (marked by orange right-pointing triangles) with $M = 1.7$ [marked by the red dashed line in Fig. 2(a)]. In the clean limit, the system hosts a normal insulator band gap with $E_g^{\text{bulk}} \approx 0.32$. With the increasing of disorder strength, the bulk energy gap monotonically decreases until the critical point $\sigma \approx 0.04$, beyond which the bulk energy gap gradually increases. The evolution of the bulk energy gap conforms to the process of gap closure and reopening, indicating that the system undergoes a TPT during the process of disorder enhancement. However, we must point out that, in our calculations, the minimum value of the bulk energy gap is not strictly equal to zero. A reasonable explanation for this issue is the presence of finite-size effects [83]. When a sufficiently large sample size is chosen, the size effects can be significantly mitigated (see Fig. 7 in Appendix A).

We also compute a line graph depicting the evolution of the real-space topological invariant spin Bott index varying with disorder strength [marked by blue circles in Fig. 2(b)], which matches well the evolution process of the bulk energy gap. It is found that the spin Bott index jumps from 0 to 1 at $\sigma \approx 0.04$ and then remains stable thereafter, with a platform without any fluctuations. Thus, it is further indicated that the topological phase transition induced by structural disorder has occurred. Furthermore, we map a line graph showing the variation of two-terminal conductance with changing disorder strength [marked by yellow left-pointing triangles in Fig. 2(b)]. As the disorder strength reaches the phase transition critical point, the conductance gradually increases from zero and approaches $2e^2/h$. Subsequently, a typical quantized conductance plateau at $G = 2e^2/h$ emerges, providing further evidence of the structural disorder-induced phase transition from a normal insulator phase to a quantum spin Hall insulator phase.

For a more intuitive presentation of the aforementioned computational results, we plot the energy spectrum and wave function distribution of the normal insulator phase as well as the disorder-induced topological insulator phase in Fig. 3. When $\sigma = 0$, the system hosts a normal insulator phase with a large energy gap under both open boundary conditions (marked by blue circles) and periodic boundary conditions (marked by red dots), as shown in Fig. 3(a). The corresponding values of the spin Bott index and conductance are equal to zero. In this scenario, the wave functions are localized in the bulk. However, when the disorder strength is set to $\sigma = 0.18$, a series of in-gap states within the bulk energy gap emerge [as shown in Fig. 3(c)], localized at the boundaries of the sample [see Fig. 3(d)], indicating that the system is now in a topological insulator phase. This computational result agrees well with the calculated values of the spin Bott index and two-terminal conductance. Therefore, the TPT from a normal insulator phase to a topological insulator phase induced by structural disorder is clearly confirmed.

IV. STRUCTURAL DISORDER-INDUCED HIGHER-ORDER TOPOLOGICAL PHASE

In this section, we concentrate on the structural disorder-induced higher-order topological phase in an Ammann-Beenker tiling quasicrystal with square and octagon boundary conditions. All calculations are based on the Hamiltonian $\mathcal{H} = H + H_g$. The introduction of the Wilson mass term H_g breaks the time-reversal symmetry and the chiral symmetry of the system, while the particle-hole symmetry is still preserved. Furthermore, we have also confirmed that

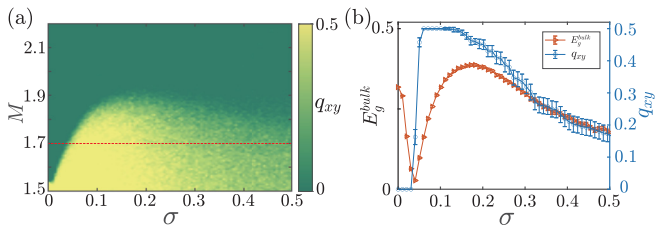

FIG. 4. (a) Topological phase diagram of the Ammann-Beenker tiling quasicrystal in (M, σ) space obtained by calculating the real-space topologically invariant quadrupole moment q_{xy}. The yellow color represents the higher-order topological insulator phase corresponding to $q_{xy} = 0.5$, and the green color represents the normal insulator phase corresponding to $q_{xy} = 0$. The red dashed line represents $M = 1.7$. (b) Bulk energy gap E_g^{bulk}, marked by orange right-pointing triangles, and quadrupole moment q_{xy}, marked by blue circles versus disorder strength σ with $M = 1.7$. The system contains 1005 sites, and 500 disorder configurations are made.

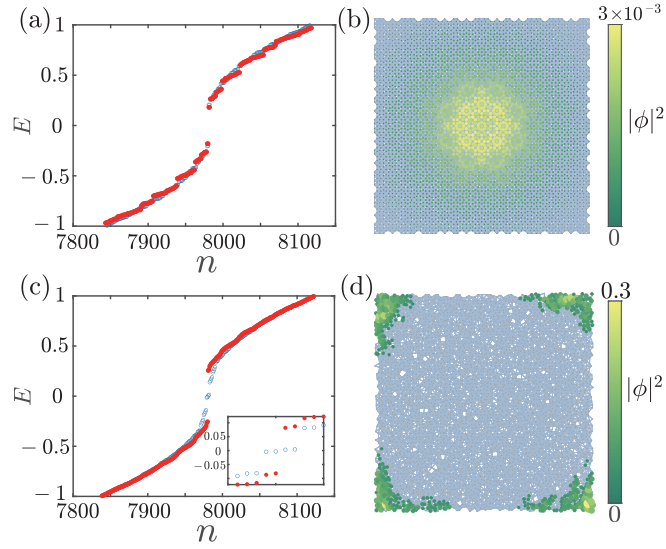

FIG. 5. (a) Energy spectrum of the normal insulator with open boundary conditions (marked by blue circles) and periodic boundary conditions (marked by red dots), corresponding to the situation with $\sigma = 0$ in Fig. 4(b). (b) The probability density of the four eigenstates which are the nearest to zero energy in (a). (c) Energy spectrum of the topological insulator corresponding to the situation with $\sigma = 0.15$ in Fig. 4(b). (d) The probability density of the four eigenstates which are the nearest to zero energy. The system size is set to contain 4061 sites, $g = 1$, and $M = 1.7$. The color bar represents the magnitude of the probability of the wave function $|\phi|^2$.

structural disorder does not lead to the breaking of particle-hole symmetry. Therefore, the real-space quadrupole moment can be quantized because it is protected by particle-hole symmetry [27].

We map out the phase diagram in (M, σ) space for the case of square boundary conditions in Fig. 4(a), where $g = 1$. The color map represents the magnitude of the real-space quadrupole moment q_{xy}. It is found that the system is in a topologically trivial phase with $q_{xy} = 0$ in the region where $1.55 < M < 2.2$ in the clean limit. With the increase of the disorder strength, the higher-order topological phase occurs with q_{xy} going from 0 to 0.5 in the region of $1.55 < M < 1.9$. The values of critical points increase monotonically with the increase of M. The structural disorder-induced higher-order insulator phases remain stable when the disorder strength is less than 0.2, beyond which the higher-order topological phases gradually break down.

In Fig. 4(b), we plot the real-space quadrupole moment q_{xy} versus disorder strength σ as well as the bulk energy gap with $M = 1.7$ shown by the red dashed line in Fig. 4(a). The system is a normal insulator phase in the clean limit characterized by $q_{xy} = 0$ and a bulk energy gap $E_g^{\text{bulk}} \approx 0.32$. With the increase of σ, in the region $0.045 < \sigma < 0.18$, a remarkable plateau of quantized $q_{xy} = 0.5$ appears, which indicates a second-order topological phase induced by structural disorder. Meanwhile, the bulk energy gap monotonically decreases until the critical point $\sigma \approx 0.045$, beyond which the bulk energy gap gradually increases. The closure and subsequent reopening of the bulk energy gap further demonstrate the structural disorder-induced topological phase. However, as the disorder strength continues to increase, the quantized quadrupole moment platform gradually disappears, accompanied by a gradual reduction of the bulk energy gap.

To verify the aforementioned computational results of the quadrupole moment and bulk energy gap, we plot the eigenspectrum and probability density of the four eigenstates which are the nearest to zero energy in Fig. 5. It can be seen that the system hosts a normal insulator phase with a large energy gap under both open boundary conditions and periodic boundary conditions, and the four eigenstates which are the nearest to zero energy are local in the bulk, as shown in Fig. 5(a). However, when the disorder strength is set to $\sigma = 0.15$, four in-gap states appear, localized at the four corners of the sample [see Figs. 5(c) and 5(d)]. These corner states are powerful proof of a structural disorder-induced higher-order topological insulator. Note that the four in-gap states are not strictly degenerate to zero owing to the finite-size effect. For a sample of finite size, the four corner states tend to overlap. In the inset in Fig. 5(c), we plot the eigenspectrum of the open lattice with 16 437 sites with $\sigma = 0.15$. We find that the energy values of the four in-gap states are approximately equal to zero energy.

In addition, we calculate the structural disorder-induced higher-order topological phase in an Ammann-Beenker tiling quasicrystal with an octagonal boundary. In Fig. 6, we plot the eigenspectrum and probability density of the eight eigenstates which are the nearest to zero energy for different disorder strengths. In the clean limit, i.e., $\sigma = 0$, the system is in a topologically trivial phase characterized by a trivial energy gap under both open (marked by blue circles) and periodic (marked by red dots) boundary conditions, with eigenstates localized in the bulk shown in Fig. 6(b). However, when the structural disorder strength is set to $\sigma = 0.13$, a second-order topological phase arises with eight topological corner states localized at the eight corners of the sample, as shown in Fig. 6(d). We believe that the higher-order topological insulator with eight corner states is a novel phase belonging exclusively to the quasicrystalline structure. The quadrupole moment q_{xy} is only available to measure the bulk quadrupole topology with square boundary conditions. A higher-order

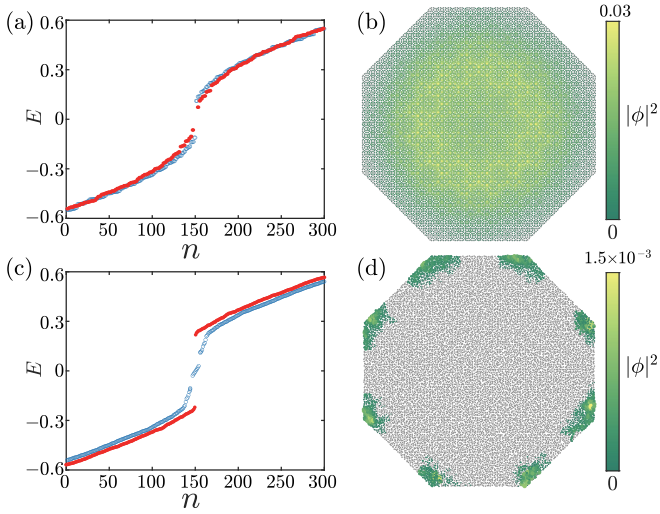

FIG. 6. (a) Energy spectrum of the normal insulator with open boundary conditions (marked by blue circles) and periodic boundary conditions (marked by red dots), where $\sigma = 0$. (b) The probability density of the eight eigenstates which are the nearest to zero energy in (a). (c) Energy spectrum of the higher-order topological insulator phase with open and periodic boundary conditions, where $\sigma = 0.13$. (d) The probability density of the eight eigenstates which are the nearest to zero energy. The system size is set to contain 13 289 sites, $g = 1.4$, and $M = 1.55$. The color bar represents the magnitude of the probability of the wave function $|\phi|^2$.

topological insulator with more than four zero-energy modes does not belong to the class of topological quadrupole insulators. Thus, it does not work for octagonal samples. It is noted that a generalized quadrupole moment has been proposed to characterize the higher-order phase in a regular octagon [84], and this method has been used to characterize the Weyl semimetal phase in a three-dimensional quasicrystal [85]. We calculate the topologically invariant generalized quadrupole moment in an octagonal quasicrystalline lattice with structural disorder (see Fig. 8 in Appendix B). The results depict the phase transition induced by structural disorder from a normal insulator to a higher-order topological insulator, which agrees well with the distribution of the wave functions. Another appropriate way to characterize the higher-order topological phase is to adopt the existence of the corner states as a working definition [29,36,80–82]. Thus, the eight corner states, induced by structural disorder in Fig. 6(d), are strong evidence of the emergence of the higher-order topological insulator.

Additionally, we would like to point out that, although we employed a relatively large lattice model in the calculation of the octagonal boundary conditions, the energy eigenvalues of the corner states still do not degenerate to zero. We attribute this to the easier overlap of two corner states along each edge of the octagon (compared to a square), which is inherently the finite-size effect. We speculate that under thermodynamic limit conditions, the eight corner states will exhibit better localization, and concurrently, their energy eigenvalues will tend to be degenerate. In addition, we suspect that the structural disorder-induced higher-order topological insulator with eight corner states arises from the rotational symmetry of the quasicrystal. Despite the local disruption of the eightfold rotational symmetry due to structural disorder, the global symmetry is still maintained on a statistical average [86–88]. Thus, it can be anticipated that the symmetry, including fourfold and eightfold rotational symmetries, disrupted by structural disorder, is statistically restored through ensemble averaging [84] and that the higher-order topological insulator phase is protected by the average global symmetry.

V. CONCLUSION

In this work, we investigated the structural disorder-induced first-order topological phase and higher-order topological phase in an Ammann-Beenker tiling quasicrystal. The quasicrystalline quantum spin Hall insulator is considered to be the fundamental model. We introduced structural disorder into the normal insulator phase which was obtained by adjusting parameters. Based on calculating the real-space spin Bott index and two-terminal conductance, we found a structural disorder-induced first-order topological insulator phase characterized by a quantized spin Bott index and quantized conductance. Additionally, the states that emerge within the bulk energy gap localized at the four edges of the sample further validated our computational results. Furthermore, we introduced the Wilson mass term to the quasicrystalline quantum spin Hall insulator to obtain a higher-order topological insulator model, and an initial state with a normal insulator phase was achieved by modifying system parameters. Based on calculating the real-space quadrupole moment, we found a structural disorder-induced higher-order topological insulator phase characterized by a quantized quadrupole moment. The corner states localized at the vertices of the sample serve as compelling evidence of the existence of higher-order topological insulators.

ACKNOWLEDGMENTS

This work was supported by a project from the NSFC (Grant No. 12122408) and the National Key R&D Program (Grant No. 2023YFB4603800). B.Z. was supported by the NSFC (Grant No. 12074107), the program of the outstanding young and middle-aged scientific and technological innovation team of the colleges and universities in Hubei Province (Grant No. T2020001), and the innovation group project of the Natural Science Foundation of Hubei Province of China (Grant No. 2022CFA012). T.P. was supported by the Doctoral Research Start-Up Fund of Hubei University of Automotive Technology (Grant No. BK202216). C.-B.H. was supported by the NSFC (Grant No. 12304539). Z.-R.L. was supported by the Postdoctoral Fellowship Program of CPSF (under Grant No. GZC20230751) and the Postdoctoral Innovation Research Program in Hubei Province (under Grant No. 351342).

APPENDIX A: FINITE-SIZE ANALYSIS

In this Appendix, we plot the bulk energy gap versus the size of the system. It has been observed that the minimum value of the bulk energy gap decreases with increasing system

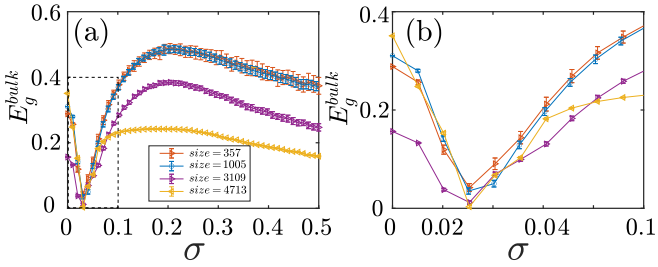

FIG. 7. (a) The bulk energy gap as a function of disorder strength σ for different system sizes. (b) An enlarged view corresponding to the dashed area in (a). An average of 400 random configurations are taken. The other parameters are the same as in Fig. 2(b).

size, as shown in Fig. 7. It can be inferred that under the conditions of the thermodynamic limit, the bulk energy gap will be closed strictly at the critical point of the phase transition.

APPENDIX B: GENERALIZED QUADRUPOLE MOMENT

In this Appendix, we plot the generalized quadrupole moment versus the strength of structural disorder in an octagonal quasicrystalline lattice. To compute the generalized quadrupole moment in an octagon, one needs to transform the position coordinates of the octagonal lattice sites [84,85]. Due to the change in site positions, the position operator should be changed accordingly. Meanwhile, the eigenvectors of occupied states should not be changed. In Fig. 8, we plot the generalized quadrupole moment versus the strength of structural disorder in an octagonal sample with different sample sizes. The system is a normal insulator phase in the clean limit characterized by $q_{xy} = 0$. With increasing disorder strength, q_{xy} increases from 0 and approaches 0.5, indicating that the system has undergone a phase transition from a trivial phase to a higher-order topological nontrivial phase.

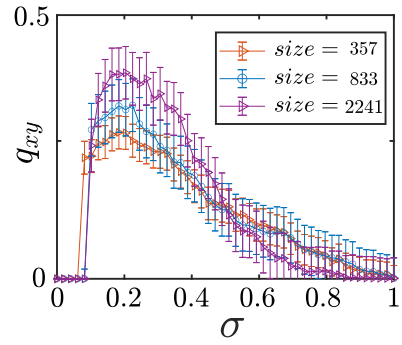

FIG. 8. The generalized quadrupole moment as a function of disorder strength for different system sizes. An average of 1000 random configurations are taken. We set $M = 1.55$ and $g = 1.4$.

[1] M. Kastner, Phase transitions and configuration space topology, Rev. Mod. Phys. **80**, 167 (2008).

[2] A. Bansil, H. Lin, and T. Das, Colloquium: Topological band theory, Rev. Mod. Phys. **88**, 021004 (2016).

[3] M. Z. Hasan and C. L. Kane, Colloquium: Topological insulators, Rev. Mod. Phys. **82**, 3045 (2010).

[4] X.-L. Qi and S.-C. Zhang, Topological insulators and superconductors, Rev. Mod. Phys. **83**, 1057 (2011).

[5] S. Longhi, Topological phase transition in non-Hermitian quasicrystals, Phys. Rev. Lett. **122**, 237601 (2019).

[6] S. Rufo, N. Lopes, M. A. Continentino, and M. A. R. Griffith, Multicritical behavior in topological phase transitions, Phys. Rev. B **100**, 195432 (2019).

[7] J. Li, R.-L. Chu, J. K. Jain, and S.-Q. Shen, Topological Anderson insulator, Phys. Rev. Lett. **102**, 136806 (2009).

[8] C. W. Groth, M. Wimmer, A. R. Akhmerov, J. Tworzydło, and C. W. J. Beenakker, Theory of the topological Anderson insulator, Phys. Rev. Lett. **103**, 196805 (2009).

[9] E. Prodan, T. L. Hughes, and B. A. Bernevig, Entanglement spectrum of a disordered topological Chern insulator, Phys. Rev. Lett. **105**, 115501 (2010).

[10] Y. Xing, L. Zhang, and J. Wang, Topological Anderson insulator phenomena, Phys. Rev. B **84**, 035110 (2011).

[11] E. V. Castro, M. P. López-Sancho, and M. A. H. Vozmediano, Anderson localization and topological transition in Chern insulators, Phys. Rev. B **92**, 085410 (2015).

[12] S. Liu, T. Ohtsuki, and R. Shindou, Effect of disorder in a three-dimensional layered Chern insulator, Phys. Rev. Lett. **116**, 066401 (2016).

[13] Y. Kuno, Disorder-induced Chern insulator in the Harper-Hofstadter-Hatsugai model, Phys. Rev. B **100**, 054108 (2019).

[14] R. Chen, D.-H. Xu, and B. Zhou, Disorder-induced topological phase transitions on Lieb lattices, Phys. Rev. B **96**, 205304 (2017).

[15] H.-M. Guo, G. Rosenberg, G. Refael, and M. Franz, Topological Anderson insulator in three dimensions, Phys. Rev. Lett. **105**, 216601 (2010).

[16] I. Mondragon-Shem, T. L. Hughes, J. Song, and E. Prodan, Topological criticality in the chiral-symmetric AIII class at strong disorder, Phys. Rev. Lett. **113**, 046802 (2014).

[17] C.-Z. Chen, J. Song, H. Jiang, Q.-F. Sun, Z. Wang, and X. C. Xie, Disorder and metal-insulator transitions in Weyl semimetals, Phys. Rev. Lett. **115**, 246603 (2015).

[18] R. Chen, D.-H. Xu, and B. Zhou, Topological Anderson insulator phase in a Dirac-semimetal thin film, Phys. Rev. B **95**, 245305 (2017).

[19] R. Chen, C.-Z. Chen, J.-H. Sun, B. Zhou, and D.-H. Xu, Phase diagrams of Weyl semimetals with competing intraorbital and interorbital disorders, Phys. Rev. B **97**, 235109 (2018).

[20] R. Chen, D.-H. Xu, and B. Zhou, Floquet topological insulator phase in a Weyl semimetal thin film with disorder, Phys. Rev. B **98**, 235159 (2018).

[21] P. V. Sriluckshmy, K. Saha, and R. Moessner, Interplay between topology and disorder in a two-dimensional semi-Dirac material, Phys. Rev. B **97**, 024204 (2018).

[22] J. Borchmann, A. Farrell, and T. Pereg-Barnea, Anderson topological superconductor, Phys. Rev. B **93**, 125133 (2016).

[23] W. Qin, D. Xiao, K. Chang, S.-Q. Shen, and Z. Zhang, Disorder-induced topological phase transitions in two-dimensional spin-orbit coupled superconductors, Sci. Rep. **6**, 39188 (2016).

[24] S. Lieu, D. K. K. Lee, and J. Knolle, Disorder protected and induced local zero-modes in longer-range Kitaev chains, Phys. Rev. B **98**, 134507 (2018).

[25] C.-B. Hua, R. Chen, D.-H. Xu, and B. Zhou, Disorder-induced Majorana zero modes in a dimerized Kitaev superconductor chain, Phys. Rev. B **100**, 205302 (2019).

[26] L.-Z. Tang, L.-F. Zhang, G.-Q. Zhang, and D.-W. Zhang, Topological Anderson insulators in two-dimensional non-Hermitian disordered systems, Phys. Rev. A **101**, 063612 (2020).

[27] C.-A. Li, B. Fu, Z.-A. Hu, J. Li, and S.-Q. Shen, Topological phase transitions in disordered electric quadrupole insulators, Phys. Rev. Lett. **125**, 166801 (2020).

[28] Y.-B. Yang, K. Li, L.-M. Duan, and Y. Xu, Higher-order topological Anderson insulators, Phys. Rev. B **103**, 085408 (2021).

[29] T. Peng, C.-B. Hua, R. Chen, Z.-R. Liu, D.-H. Xu, and B. Zhou, Higher-order topological Anderson insulators in quasicrystals, Phys. Rev. B **104**, 245302 (2021).

[30] Y.-B. Yang, J.-H. Wang, K. Li, and Y. Xu, Higher-order topological phases in crystalline and non-crystalline systems: A review, J. Phys.: Condens. Matter **36**, 283002 (2024).

[31] E. J. Meier, F. A. An, A. Dauphin, M. Maffei, P. Massignan, T. L. Hughes, and B. Gadway, Observation of the topological anderson insulator in disordered atomic wires, Science **362**, 929 (2018).

[32] S. Stützer, Y. Plotnik, Y. Lumer, P. Titum, N. H. Lindner, M. Segev, M. C. Rechtsman, and A. Szameit, Photonic topological Anderson insulators, Nature (London) **560**, 461 (2018).

[33] G.-G. Liu *et al.*, Topological Anderson insulator in disordered photonic crystals, Phys. Rev. Lett. **125**, 133603 (2020).

[34] X. Cui, R.-Y. Zhang, Z.-Q. Zhang, and C. T. Chan, Photonic $\mathbb{Z}_2$ topological Anderson insulators, Phys. Rev. Lett. **129**, 043902 (2022).

[35] F. Zangeneh-Nejad and R. Fleury, Disorder-induced signal filtering with topological metamaterials, Adv. Mater. **32**, 2001034 (2020).

[36] W. Zhang, D. Zou, Q. Pei, W. He, J. Bao, H. Sun, and X. Zhang, Experimental observation of higher-order topological Anderson insulators, Phys. Rev. Lett. **126**, 146802 (2021).

[37] K. Li, J.-H. Wang, Y.-B. Yang, and Y. Xu, Symmetry-protected topological phases in a Rydberg glass, Phys. Rev. Lett. **127**, 263004 (2021).

[38] J.-H. Wang, Y.-B. Yang, N. Dai, and Y. Xu, Structural-disorder-induced second-order topological insulators in three dimensions, Phys. Rev. Lett. **126**, 206404 (2021).

[39] C. Wang, T. Cheng, Z. Liu, F. Liu, and H. Huang, Structural amorphization-induced topological order, Phys. Rev. Lett. **128**, 056401 (2022).

[40] R. Zallen, *The Physics of Amorphous Solids* (Wiley, New York, 2008).

[41] M. H. Cohen and D. Turnbull, Metastability of amorphous structures, Nature (London) **203**, 964 (1964).

[42] P. Duwez, R. H. Willens, and W. Klement, Jr., Continuous series of metastable solid solutions in silver-copper alloys, J. Appl. Phys. **31**, 1136 (1960).

[43] H. Jones, The status of rapid solidification of alloys in research and application, J. Mater. Sci. **19**, 1043 (1984).

[44] A. Inoue, K. Ohtera, and T. Masumoto, New amorphous Al-Y, Al-La and Al-Ce alloys prepared by melt spinning, Jpn. J. Appl. Phys. **27**, L736 (1988).

[45] H. Chen and D. Turnbull, Formation and stability of amorphous alloys of Au-Ge-Si, Acta Metall. **18**, 261 (1970).

[46] L. Schultz, Formation of amorphous metals by mechanical alloying, Mater. Sci. Eng. **97**, 15 (1988).

[47] D. B. Graves, Plasma processing, IEEE Trans. Plasma Sci. **22**, 31 (1994).

[48] C.-T. Toh *et al.*, Synthesis and properties of free-standing monolayer amorphous carbon, Nature (London) **577**, 199 (2020).

[49] C. Wang, F. Liu, and H. Huang, Effective model for fractional topological corner modes in quasicrystals, Phys. Rev. Lett. **129**, 056403 (2022).

[50] R. Chen, C.-Z. Chen, J.-H. Gao, B. Zhou, and D.-H. Xu, Higher-order topological insulators in quasicrystals, Phys. Rev. Lett. **124**, 036803 (2020).

[51] C.-B. Hua, R. Chen, B. Zhou, and D.-H. Xu, Higher-order topological insulator in a dodecagonal quasicrystal, Phys. Rev. B **102**, 241102(R) (2020).

[52] R. Chen, D.-H. Xu, and B. Zhou, Topological anderson insulator phase in a quasicrystal lattice, Phys. Rev. B **100**, 115311 (2019).

[53] L.-Z. Tang, S.-N. Liu, G.-Q. Zhang, and D.-W. Zhang, Topological Anderson insulators with different bulk states in quasiperiodic chains, Phys. Rev. A **105**, 063327 (2022).

[54] Y.-P. Wu, L.-Z. Tang, G.-Q. Zhang, and D.-W. Zhang, Quantized topological Anderson-Thouless pump, Phys. Rev. A **106**, L051301 (2022).

[55] T. Peng, C.-B. Hua, R. Chen, D.-H. Xu, and B. Zhou, Topological Anderson insulators in an Ammann-Beenker quasicrystal and a snub-square crystal, Phys. Rev. B **103**, 085307 (2021).

[56] C.-B. Hua, Z.-R. Liu, T. Peng, R. Chen, D.-H. Xu, and B. Zhou, Disorder-induced chiral and helical Majorana edge modes in a two-dimensional Ammann-Beenker quasicrystal, Phys. Rev. B **104**, 155304 (2021).

[57] V. Regis, V. Velasco, M. B. Silva Neto, and C. Lewenkopf, Structure-driven phase transitions in paracrystalline topological insulators, arXiv:2312.08779.

[58] H. Huang and F. Liu, Quantum spin Hall effect and spin Bott index in a quasicrystal lattice, Phys. Rev. Lett. **121**, 126401 (2018).

[59] H. Huang and F. Liu, Theory of spin Bott index for quantum spin Hall states in nonperiodic systems, Phys. Rev. B **98**, 125130 (2018).

[60] R. Landauer, Electrical resistance of disordered one-dimensional lattices, Philos. Mag. **21**, 863 (1970).

[61] M. Büttiker, Absence of backscattering in the quantum Hall effect in multiprobe conductors, Phys. Rev. B **38**, 9375 (1988).

[62] D. S. Fisher and P. A. Lee, Relation between conductivity and transmission matrix, Phys. Rev. B **23**, 6851 (1981).

[63] W. A. Wheeler, L. K. Wagner, and T. L. Hughes, Many-body electric multipole operators in extended systems, Phys. Rev. B **100**, 245135 (2019).

[64] C.-A. Li and S.-S. Wu, Topological states in generalized electric quadrupole insulators, Phys. Rev. B **101**, 195309 (2020).

[65] B. Kang, K. Shiozaki, and G. Y. Cho, Many-body order parameters for multipoles in solids, Phys. Rev. B **100**, 245134 (2019).

[66] A. Agarwala, V. Juričić, and B. Roy, Higher-order topological insulators in amorphous solids, Phys. Rev. Res. **2**, 012067(R) (2020).

[67] B. Grünbaum and G. C. Shephard, *Tilings and Patterns* (W. H. Freeman, New York, 1987).

[68] F. Beenker, *Algebraic Theory of Non-Periodic Tilings of the Plane by Two Simple Building Blocks: A Square and a Rhombus* (Eindhoven University of Technology, Eindhoven, 1982).

[69] M. Duneau, Approximants of quasiperiodic structures generated by the inflation mapping, J. Phys. A **22**, 4549 (1989).

[70] P. Kramer and Z. Papadopolos, *Coverings of Discrete Quasiperiodic Sets: Theory and Applications to Quasicrystals*, Vol. 180 (Springer, Berlin, 2003).

[71] A. Altland and M. R. Zirnbauer, Nonstandard symmetry classes in mesoscopic normal-superconducting hybrid structures, Phys. Rev. B **55**, 1142 (1997).

[72] A. P. Schnyder, S. Ryu, A. Furusaki, and A. W. W. Ludwig, Classification of topological insulators and superconductors in three spatial dimensions, Phys. Rev. B **78**, 195125 (2008).

[73] B. A. Bernevig, T. L. Hughes, and S.-C. Zhang, Quantum spin Hall effect and topological phase transition in HgTe quantum wells, Science **314**, 1757 (2006).

[74] X. Cheng, T. Qu, L. Xiao, S. Jia, J. Chen, and L. Zhang, Topological Anderson amorphous insulator, Phys. Rev. B **108**, L081110 (2023).

[75] A. MacKinnon, The calculation of transport properties and density of states of disordered solids, Z. Phys. B **59**, 385 (1985).

[76] G. Metalidis and P. Bruno, Green's function technique for studying electron flow in two-dimensional mesoscopic samples, Phys. Rev. B **72**, 235304 (2005).

[77] H. Tsunetsugu, T. Fujiwara, U. Kazuo, and T. Tokihiro, Eigenstates in 2-dimensional Penrose tiling, J. Phys. Soc. Jpn. **55** (1986).

[78] H. Tsunetsugu, T. Fujiwara, K. Ueda, and T. Tokihiro, Electronic properties of the Penrose lattice. I. Energy spectrum and wave functions, Phys. Rev. B **43**, 8879 (1991).

[79] O. Entin-Wohlman, M. Kléman, and A. Pavlovitch, Penrose tiling approximants, J. Phys. (Paris) **49**, 587 (1988).

[80] H. Araki, T. Mizoguchi, and Y. Hatsugai, Phase diagram of a disordered higher-order topological insulator: A machine learning study, Phys. Rev. B **99**, 085406 (2019).

[81] T. Peng, C.-B. Hua, R. Chen, Z.-R. Liu, H.-M. Huang, and B. Zhou, Density-driven higher-order topological phase transitions in amorphous solids, Phys. Rev. B **106**, 125310 (2022).

[82] Z.-R. Liu, C.-B. Hua, T. Peng, R. Chen, and B. Zhou, Higher-order topological insulators in hyperbolic lattices, Phys. Rev. B **107**, 125302 (2023).

[83] B. Zhou, H.-Z. Lu, R.-L. Chu, S.-Q. Shen, and Q. Niu, Finite size effects on helical edge states in a quantum spin-Hall system, Phys. Rev. Lett. **101**, 246807 (2008).

[84] Y.-L. Tao, J.-H. Wang, and Y. Xu, Average symmetry protected higher-order topological amorphous insulators, SciPost Phys. **15**, 193 (2023).

[85] Y.-F. Mao, Y.-L. Tao, J.-H. Wang, Q.-B. Zeng, and Y. Xu, Higher-order topological insulators and semimetals in three dimensions without crystalline counterparts, Phys. Rev. B **109**, 134205 (2024).

[86] J. Zhang, Z.-Q. Zhang, S.-g. Cheng, and H. Jiang, Topological Anderson insulator via disorder-recovered average symmetry, Phys. Rev. B **106**, 195304 (2022).

[87] L. Fu and C. L. Kane, Topology, delocalization via average symmetry and the symplectic Anderson transition, Phys. Rev. Lett. **109**, 246605 (2012).

[88] N. Yoshioka, Y. Akagi, and H. Katsura, Learning disordered topological phases by statistical recovery of symmetry, Phys. Rev. B **97**, 205110 (2018).